

# Inclusion of Levodopa into $\beta$ -Cyclodextrin: A Comprehensive Computational Study

Morteza Rezaeisadat, Nafiseh Salehi, and Abdol-Khalegh Bordbar\*

Cite This: *ACS Omega* 2021, 6, 23814–23825

Read Online

ACCESS |



Metrics &amp; More

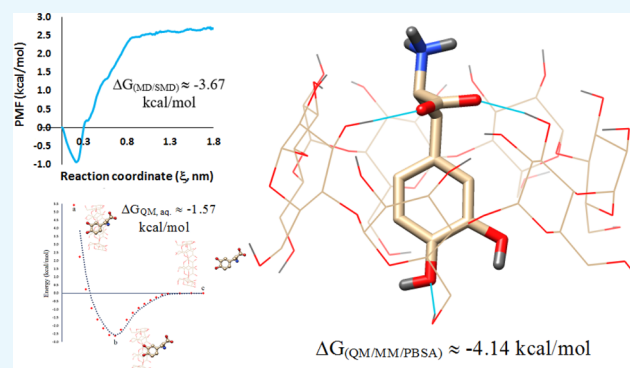


Article Recommendations



Supporting Information

**ABSTRACT:** This study focused on the inclusion of levodopa (LVDP) into  $\beta$ -cyclodextrin (BCD) using various computational methods such as quantum mechanics (QM), molecular dynamics/steered molecular dynamics (MD/SMD), and QM/molecular mechanics/Poisson–Boltzmann surface area (QM/MM/PBSA). The QM results assigned the most significant charge-transfer atoms and the higher stability of LVDP in the aqueous phase. The MD results indicate the formation of a 1:1 complex with a reasonable estimation of the effective radius of the complex, the significant contribution of hydrogen bonding in the binding energy, and the enhancement of the water solubility of LVDP. By accounting for the water hydrogen bonds and their dipolar effects, QM/MM calculations lead to the more accurate IR spectrum and binding energy of the BCD–LVDP complex. By considering carboxylic and amine functional groups' more precise arrangement, QM/MM assigns stronger hydrogen bonds between LVDP and BCD. While all the methods provide a reasonable estimation of the binding energy, the most accurate value (−4.14 kcal/mol) is obtained from QM/MM/PBSA.



## 1. INTRODUCTION

Today, a chemical drug that is a type of precursor and is known as Levodopa (LVDP) and L-Dopa (Figure 1a) is used and prescribed as a medicine for Parkinson's disease. Parkinson's disease is one of the most common diseases in different parts of the world that mostly appear in old age.<sup>1,2</sup> LVDP was able to cause immediate improvement in patients with Parkinson disease due to its conversion to dopamine in both the central nervous system and the peripheral nervous system.<sup>3–5</sup> However, excessive amounts of this drug can cause side effects such as tremors and dyskinesia. The poor aqueous solubility (3.3 mg/mL) and the degree of dissolution of LVDP are two critical factors that affect its formulation and development process and limit its therapeutic index. Therefore, we need to use a suitable drug delivery system to overcome these shortcomings.<sup>6–8</sup> Drug delivery is a process for the proper transfer of medicinal compounds into the target, to increase therapeutic efficacy, to reduce toxicity, to reduce side effects, and to increase solubility.<sup>9,10</sup> Cyclodextrins (CDs) as highly biocompatible molecules with a hydrophilic outer surface and lipophilic cavity are one of the most popular drug carriers that are widely used in the pharmaceutical industry.<sup>11,12</sup> They have the shape of a truncated cone because of the chair conformation of glucopyranose units among natural cyclodextrins ( $\alpha$ -,  $\beta$ -, and  $\gamma$ -CDs, consisting of 6, 7, and 8 glucopyranose units, respectively).<sup>13</sup>  $\beta$ -Cyclodextrin (BCD) (Figure 1b) is the best drug carrier candidate for a variety of

drugs due to the perfect cavity size, efficient drug complexation and loading, availability, and relatively low cost preparation.<sup>14</sup> The complexation of LVDP with BCD has been experimentally investigated by several research groups, indicating the formation of a 1:1 complex with favorable free binding energy ( $\Delta G_b$ ) that enhances the solubility, bioavailability, and stability of LVDP.<sup>15,16</sup> These results indicate that BCDs are promising drug delivery systems for this study.

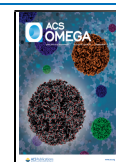
Computational methods such as quantum methods, molecular dynamics (MD), and hybrid quantum mechanics/molecular mechanics (QM/MM) provide reasonable predictions for the researcher in examining the chemical systems and reveal some of the molecular details that could not be assigned in the experimental methods.<sup>17,18</sup> There are many studies that evaluated the performance of these methods.<sup>15,19–25</sup>

Among these methods, QM methods based on solving the Schrodinger equation are the most accurate. However, due to the high computational cost, they can be applied for systems with a small number of atoms.<sup>26</sup> These methods are essential

Received: May 20, 2021

Accepted: July 5, 2021

Published: September 7, 2021



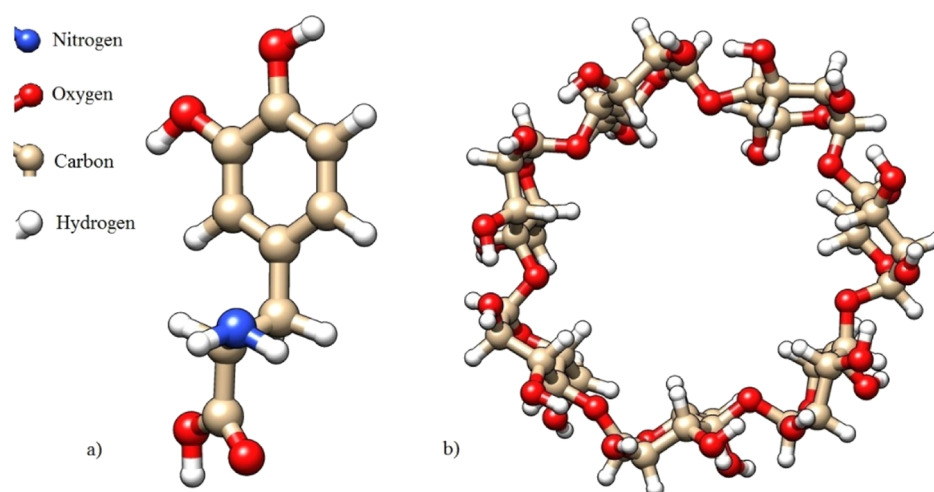


**Figure 1.** Chemical structure of (a) LVDP and (b) BCD.

in studying the properties of the electronic structure. MD methods are based on solving Newton's second law equation. They have a relatively high speed and a low computational cost that make them a good fit for evaluating systems with many atoms. This method provides good predictions about the system's mass characteristics but could not be used to study processes involving electronic transfers. However, QM/MM, as a hybrid method, has the most advantages of QM and MD methods but still has a high computational cost. In drug-BCD studies, as many-atom systems, QM methods are rarely used, and most MD methods and sometimes hybrid methods are usually applied.<sup>19,23</sup>

Although there is no comprehensive computational study on BCD–LVDP, we have performed such a study in this endeavor. For this purpose, several computational methods such as QM, MD/steered molecular dynamics (SMD), and QM/MM/Poisson–Boltzmann surface area (PBSA) have been used in parallel and comparatively. The complete results of this study reveal the molecular and energetic details of the BCD–LVDP complex and show how BCD could improve the bioavailability and solubility of LVDP. Moreover, according to the experimental results, the accuracy of the applied methods has been assessed and compared confidently.

## 2. COMPUTATIONAL METHODS

**2.1. Quantum Mechanics.** Initial geometries of LVDP (CID: 6047) and BCD (CID: 444041) are obtained from the PubChem site.<sup>27</sup> All structures are fully optimized using the modified density functional theory with the CAM-B3LYP function.<sup>28</sup> CAM-B3LYP is a hybrid exchange–correlation functional that combines B3LYP at short range with an increasing level of exact Hartree–Fock exchange at long range.<sup>29</sup> The double zeta split valence polarization with diffuse basis set functions (aug-ccpVDZ) was applied for all atoms.<sup>30</sup> To perform calculations in the aqueous phase, the conductor-like polarizable continuum model (CPCM) is used as a common water model. This is a kind of PCM that considers the charge-transfer effect as a part of solvation.<sup>31</sup> Some parameters such as structural properties, charge transfer, binding energy, electrostatic potential, normal vibrational frequency, molecular orbitals, and natural bond orbital (NBO) analysis related to LVDP, BCD, and the complex were investigated by the QM method. For quantum

calculations, Gaussian09<sup>32</sup> software has been used, and for visualization, Avogadro,<sup>33</sup> Gausview06,<sup>34</sup> and Chimera<sup>35</sup> software have been used. At first, according to the drug and NBO data's optimized structure, the electronic properties of LVDP, such as partial charge distribution, bonding lengths and angles, dipole momentum, and energies, are estimated. Then, by considering the optimized structure of BCD in the vicinity of LVDP, the binding energy is calculated. The scan calculations were performed to confirm the optimization step. The interacted points in LVDP and BCD are explored using the electrostatic potential map. Frequency calculations for LVDP identification in the BCD–LVDP spectrum were applied in both phases in accordance with the optimization method.<sup>18,19</sup> Finally, the nature of the interaction is evaluated through NBO calculations.

**2.2. Molecular Dynamics.** All MD simulations are carried out with the GROMACS-2016 package<sup>36</sup> using AMBER99SB<sup>37</sup> as a force field and SPC/E as a flexible water model.<sup>38</sup> The GROMACS package analysis tools are used to interpret the dynamics data where all simulation snapshots are visualized by VMD software.<sup>39</sup> Initial parameters of LVDP and BCD for the AMBER99SB force field were determined using the TLEAP utility implanted in AmberTools18.<sup>40</sup> In general, we used a cubic box and periodic boundary conditions in all simulations. The box lengths are chosen from 5 to 7 nm corresponding to the number of species. All species are randomly placed inside the simulation box. The following steps were considered for all simulations: (1) energy minimization (EM), (2) NVT equilibration, (3) NPT equilibration, and (4) MD production. For EM, we used the steepest descent algorithm with 50,000 steps. A middle-temperature coupling using a velocity-rescale<sup>41</sup> thermostat with a coupling constant of 0.1 ps and a middle-pressure coupling using a Berendsen barostat<sup>42</sup> with a coupling constant of 1.0 ps were applied for NVT, NPT, and MD runs. The reference temperature and pressure are 298 K and 1 atm, respectively. A cutoff radius of 1.4 nm is adopted for nonbonded interactions, short-range electrostatics, and short-range neighbor lists. However, the long-range electrostatics is handled by the particle mesh Ewald (PME) method.<sup>43</sup> Vibrations of bonds containing hydrogen atoms are constrained using a LINCS algorithm.<sup>44</sup> The leap-frog algorithm is employed for integrating Newton's equations of motion with a 2.0 fs time step. The neighbor lists are updated automatically (due to CUDA processing) every 40

times in the equilibration and production runs. The *NVT* and *NPT* equilibrium stages consist of 1.0 and 10.0 ns run times, respectively. The MD production stage consists of a 100 ns run time. The trajectories are stored every 5 ps. The quantities such as radius of gyration ( $R_g$ ), solvent accessible surface area (SASA), radial distribution function (RDF)  $g(r)$ , hydrogen bond, and principal axes of inertia are calculated based on the output data (trajectory). The binding energy in the previous step is obtained as the energy difference between the product and the raw materials. However, in this step, the bonding energy is derived from the potential of mean force (PMF), which is obtained from a series of sequence simulations, which is known as Umbrella Sampling or SMD.<sup>45,46</sup> In this method, after the system reaches equilibrium, we allow the center of mass (COM) of the molecule (LVDP) to move through the center of BCD to obtain a series of distances related to the potential energy curve. Next, we extract about 400 frames from the obtained trajectory. Considering the calculated BCD–LVDP distance for each frame, only 32 frames that show appropriate variation in the distance are selected. Then, for each of the 32 selected frames, we run a 10 ns simulation. Finally, we use the weighted histogram analysis method (WHAM)<sup>47</sup> to extract the PMF and  $\Delta G_b$ .

**2.3. Hybrid Method (QM/MM).** After MD simulation for 100 ns, the QM/MM computations were carried out to ensure that the system was in equilibrium. For QM/MM computation, Gromacs2016 and ORCA software were compiled together using a modified script.<sup>48</sup> A 10 ns QM/MM simulation was performed, which obtained 200 snapshots from the last 5 ns to calculate the binding energy and investigate the system dynamics.

In the QM/MM method, LVDP is described quantum mechanically (B3LYP/6-31G\*), while its environment, which consists of BCD and the water solvent, is described molecular mechanically (Amber99SB force field). A QM calculation is performed for LVDP using electronic embedding that describes the electrostatic interactions between the electrons of the QM region and the MM atoms and between the QM nuclei and the MM atoms included in the Hamiltonian for the QM subsystem.<sup>49</sup> Nonelectrostatic interactions between the QM and MM subsystems are calculated through a Lennard-Jones potential using parameters from the classical force field.<sup>50,51</sup> Single-point interaction energy calculations based on the time averaged and changes in the internal properties of the LVDP structure were examined for each of the snapshots obtained from the QM/MM MD calculations. The binding energy of BCD–LVDP was calculated using a QM/MM/PBSA method that was externally implemented in GRO-MACS.<sup>52</sup> As the entropy contribution is not considered in this method, the normal mode frequency, which requires the calculation of eigenvectors in the Hessian matrix, is used to estimate the entropy. As usual, the binding energy was defined as follows:<sup>53</sup>

$$G_{\text{binding}} = E_{\text{complex}} + E_{\text{solvation}} - T\Delta S \quad (1)$$

where  $E_{\text{complex}}$ ,  $E_{\text{solvation}}$ , and  $T\Delta S$  are the interaction energy, solvation energy, and entropy contribution for forming BCD–LVDP from its separated constituents, respectively, and using the QM/MM level for estimation of  $G_{\text{binding}}$  leads to a more accurate value.

### 3. RESULTS AND DISCUSSION

In this study, we used CPCM as an implicit water model to evaluate the behavior of drugs and drug carriers in an aqueous environment. The LVDP molecule is optimized in both gas and aqueous media (pH  $\approx$  7), and the schematic representation of the optimized structures and the relevant electronic structural properties are shown in Figure 2 and

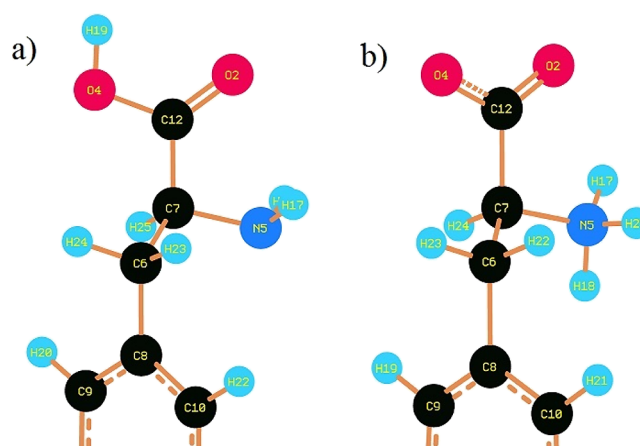


**Figure 2.** Optimized structure of LVDP in (a) gas phase and (b) aqueous media.

Tables 1, and 2, respectively. It should be mentioned that the predicted structure and ionization state of LVDP in the aqueous phase by ChemAxon software has been used as the initial structure for final optimization by Gaussian.

According to Table 1, the most significant change in the estimated partial atomic charge from NBO calculations, as an index of charge transfer from the gas phase to the aqueous medium, refers to the oxygen atom of the carboxyl group (O2) and the nitrogen atom of the amino group (NS). However, the lowest charge transfer belongs to alpha carbon in the amino acid group (C7). C12–O4 shows the most significant change in the carboxylic acid group regarding bond lengths, which represents the increase of bond order in the aqueous media. The lower value of LVDP's chemical potential, as an index of electronic structure stability, in the aqueous phase (−3.03 kcal/mol) in comparison to the gas phase (−2.88 kcal/mol), represents the higher stability of LVDP in the aqueous phase. The higher value of the energy gap in the aqueous phase (4.54 kcal/mol) concerning the gas phase (4.48 kcal/mol) also represents the higher stability in the aqueous phase, in agreement with the chemical potential results.

In the next step, the interaction of LVDP with BCD is investigated in both gas and aqueous phases using the optimized LVDP structure. There is a significant difference between the binding energies in the gas (0.03 kcal/mol) and aqueous (−1.57 kcal/mol) phases, which could be attributed to electrostatic interactions and hydrogen bonding in the aqueous medium, which are discussed below. Usually, for a more detailed study of the optimized structure and energy, the two components of the complex are placed at different distances, and the complex's energy changes are evaluated. As shown in Figure 3, the potential energy curve obtained from the displacement of the LVDP molecule in the Z-axis has the lowest amount of energy at the optimal point (Figure 3b). As the phenolic groups of the drug approach the narrow head of BCD, the energy level increases sharply due to the increase of

**Table 1. Some Properties Such as Charges, Lengths, Angles, and Dihedral Angles of the Optimized Structure of LVDP**

	charge ( $-e$ )		length ( $\text{\AA}$ )		angle (deg)			
	isolate	aqueous	isolate	aqueous	isolate	aqueous		
O2	-0.670	-0.823	H17-N5	1.019	1.030	C8-C6-C7	113.676	113.591
O4	-0.726	-0.811	N5-C7	1.457	1.511	C6-C7-C12	108.245	115.716
N5	-0.910	-0.764	C6-C7	1.554	1.539	C12-C7-N5	113.488	109.432
C6	-0.443	-0.456	C6-C8	1.513	1.517	C8-C6-C7-C12	10.063	1.009
C7	-0.142	-0.138	C7-C12	1.530	1.524	C8-C6-C7-N5	65.865	55.011
C8	-0.059	-0.095	C12-O2	1.216	1.218	N5-C7-C12-O2	23.973	12.954
C12	0.857	0.805	C12-O4	1.351	1.218	N5-C7-C12-O4	22.945	1.118

**Table 2. Some Electronic Properties Related to LVDP in the Gas and Aqueous Media**

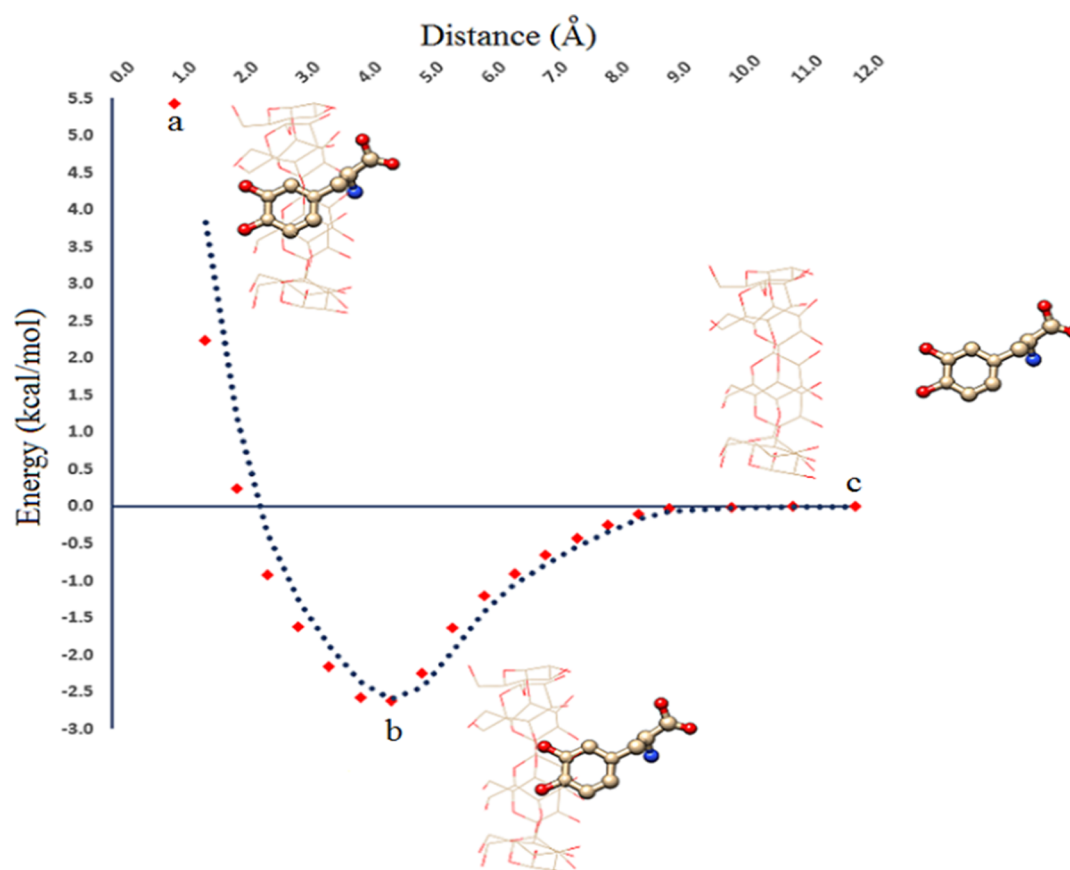
properties	isolate	aqueous
$E$ (hartree)	-705.27	-705.29
$E_{\text{LUMO}}$ (eV)	-0.027	-0.033
$E_{\text{HOMO}}$ (eV)	-0.222	-0.230
momentum (debye)	2.07	16.62

the electrostatic repulsion (Figure 3a). Furthermore, as the phenolic groups move away from the wide head of BCD, the strength of the interactions decreases, resulting in zero energy (Figure 3c). On the other hand, the drug molecule rotation in BCD does not cause more change in energy.

The molecular electrostatic potential method (MEP) is an efficient computational tool used to estimate the potential energy surface as an essential indicator in molecular interactions and chemical reactions.<sup>54,55</sup> Figure S1 is the

molecular electrostatic potential map of BCD and LVDP molecules. As shown in Figure S1a, the inner surface of BCD has hydrophobic properties due to its low electrostatic potential (neutral charge distribution) and its outer surface due to its high electrostatic potential (positive and negative charge distribution) has hydrophilic properties. Also, in the LVDP molecule, the amide group has hydrophilicity due to its high electrostatic potential, and the phenolic group shows hydrophobicity due to benzene ring groups. Therefore, the drug molecule will approach the inner surface of BCD from the phenolic group.

Harmonic vibrational frequencies corresponding to the optimized BCD structure were calculated in the presence and absence of LVDP in the gas phase. Figure 4, as IR spectra of BCD and BCD-LVDP, shows the results. The red, blue, and green spectra are related to BCD, BCD-LVDP, and LVDP in the aqueous phase, respectively. As can be seen in the blue spectrum, the specific peaks in points a, b, c, d, e, and f are

**Figure 3.** Energy scanning from the displacement of the LVDP molecule in the Z-axis.

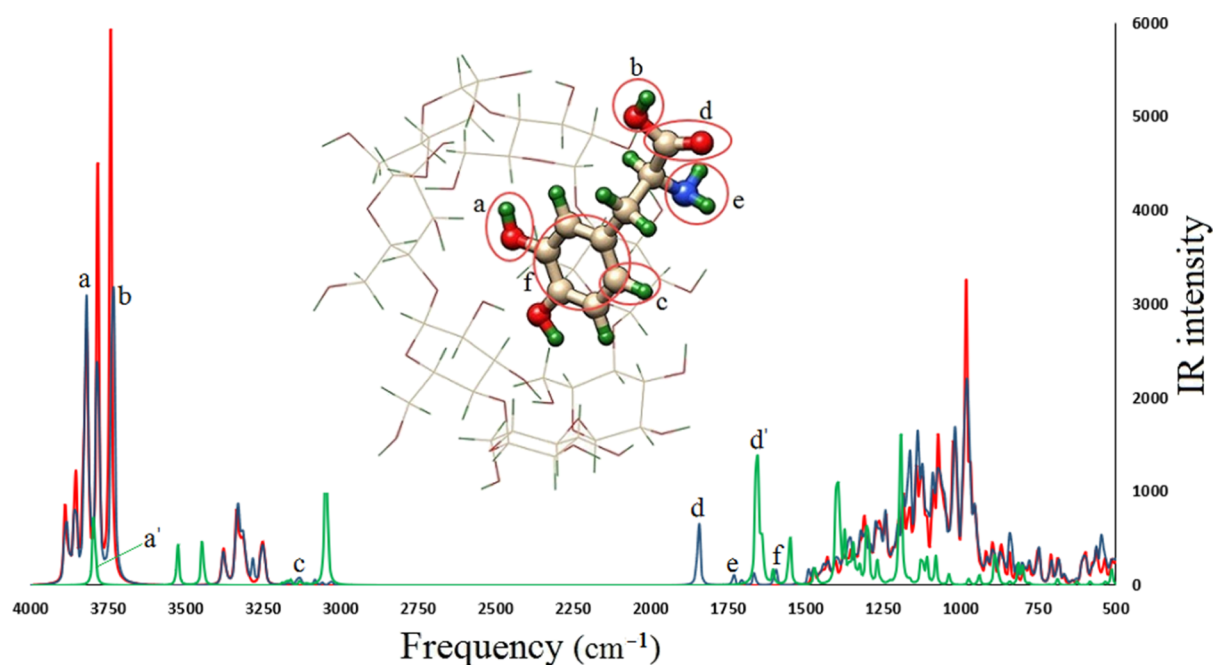


**Figure 4.** Gas-phase IR spectra of BCD (red) and BCD–LVDP (blue) and the aqueous-phase IR spectrum of LVDP (green). The inner scheme represents the structure of BCD–LVDP. The bonds in the scheme and the corresponding peaks in the spectrum are assigned with the same letter.

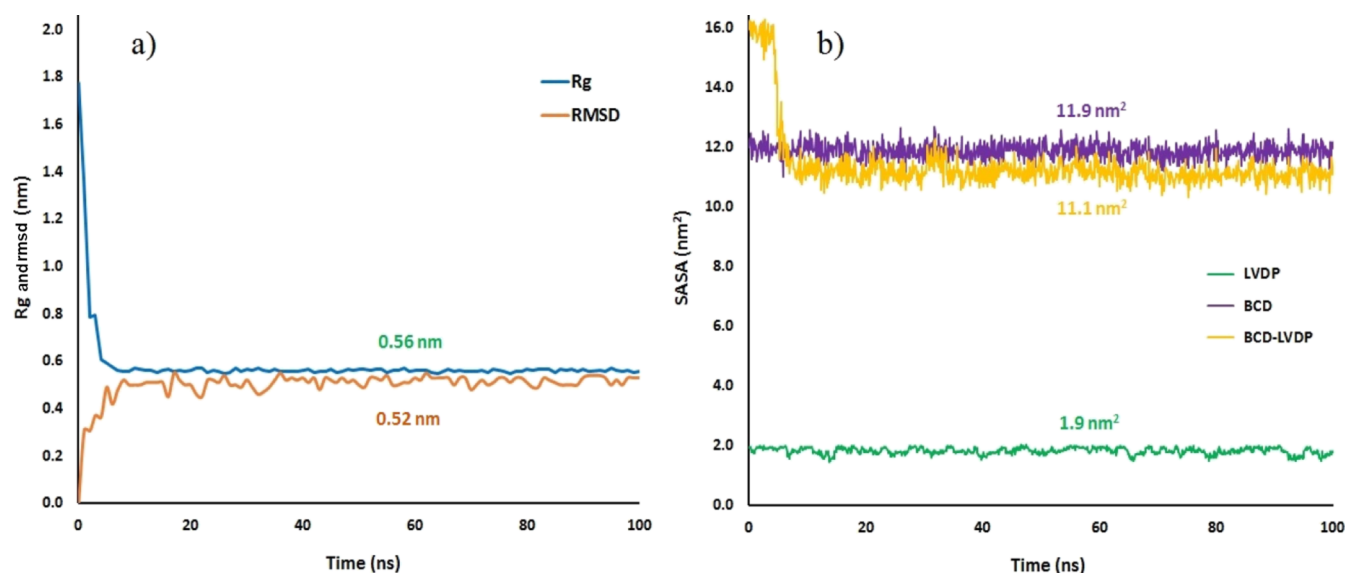


**Figure 5.** (a) Diagrams of the rmsd and the radius of gyration ( $R_g$ ) in 100 ns simulation of BCD–LVDP; (b) variation of SASA vs simulation time for LVDP, BCD, and BCD–LVDP. The average values in the last 20 ns are reported in the curve.

related to the presence of LVDP. The inconsistency of the calculated bond frequencies with the experimental values could be related to the nonconsidering of intermolecular interactions and the solvent effect in the gas phase. For instance, the peak related to the frequency of free O–H bond stretching in phenol groups is usually observed in the range of 3600 to 3650 ( $\text{cm}^{-1}$ ),<sup>56</sup> while the value of 3801  $\text{cm}^{-1}$  (no scaled) is estimated for this frequency [peak (a) in Figure 4]. The other specified peaks are also listed in Table 4. The difference between the observed values and the expected values is higher for the more polar bonds that could be related to not considering intermolecular interactions in the gas phase.<sup>57</sup>

The transferred charge quantity from a donor–acceptor orbital and its stability are estimated using the second-order

perturbation theory, which is implemented in NBO calculations. The results are listed in Table S1. The low values of intermolecular charge transfer (Nos. 5, 6, and 7) represent the weak hydrogen bonds between BCD and LVDP and the predominant role of electrostatic interactions in the binding energy.

In the next step, the interaction of LVDP with BCD is investigated in MD simulation. Two main parameters are used to evaluate the system equilibrium conditions, which are root-mean-square deviation (RMSD) and radius of gyration ( $R_g$ ). rmsd is a measure of the amount of displacement between atoms or different groups over time and is usually used as the main parameter in the equilibrium of molecular dynamic systems.  $R_g$  is also used as a measure of collapse in some

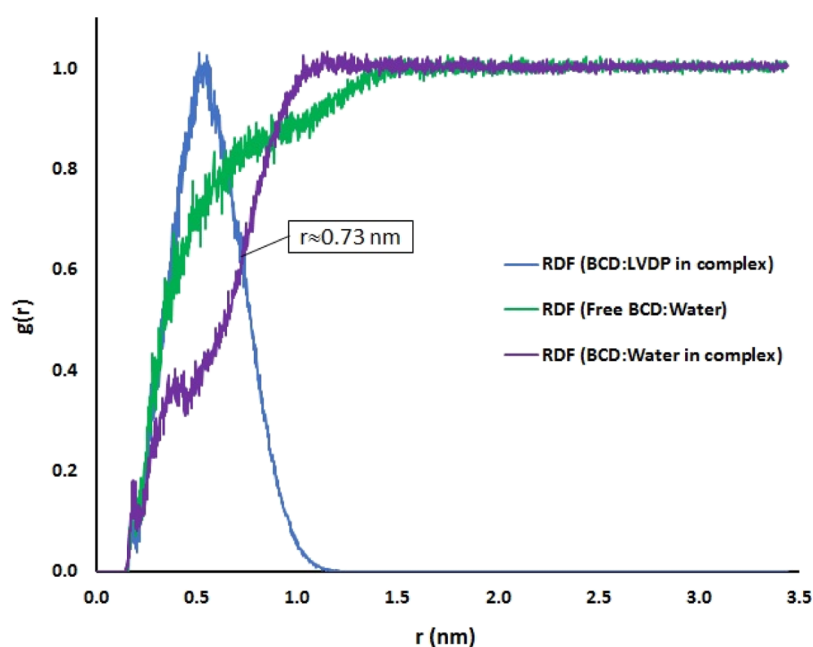


**Figure 6.** Normal RDF calculation for pair molecules.

structures such as proteins, polymers, and micelle formation.<sup>58,59</sup> The 100 ns time regime of the calculated rmsd and  $R_g$  are shown in Figure 5a. The fluctuations have been substantially decreased for both parameters after the 8 ns simulation that guarantees the achievement of equilibrium after 100 ns. The mean values of rmsd and  $R_g$  in the last 20 ns simulation are 0.52 and 0.56 nm, respectively. The effective radius ( $R_s$ ) that is related to  $R_g$  by  $R_s \approx 1.3R_g$ <sup>60,61</sup> equals 0.73 nm (7.3 Å).

Another parameter attributed to solubility is the SASA;<sup>62,63</sup> as the SASA goes up, this means that a compound solubility increases, or if something is complexed by BCD, we would expect the higher SASA. The time variation of SASA for LVDP, BCD, and BCD–LVDP is given in Figure 5b. The least average value of 1.9 nm<sup>2</sup> belongs to LVDP, indicating the least aqueous solubility ( $\approx 3.3$  mg/mL), while the highest average value of 11.9 nm<sup>2</sup> is for BCD, representing the highest aqueous solubility ( $\approx 18.2$  mg/mL). The higher value of SASA for BCD–LVDP (11.1 nm<sup>2</sup>) with respect to LVDP, representing the solubility of LVDP, goes up due to the complexation with BCD. The lower value of SASA for BCD–LVDP (11.1 nm<sup>2</sup>) concerning the free BCD (11.9 nm<sup>2</sup>) could be due to the water replacement by LVDP in the inner cavity of BCD. The water displacement will be further investigated by calculating the normal RDF of water in the subsequent section. However, these results show up the appropriate BCD for the complexation of LVDO and enhancement of its aqueous solubility.

The normal distribution of LVDP around BCD and water molecules around BCD and LVDP have been examined in the next step. For this purpose, the normal RDF module, which considers the COM of the molecules, has been used. The variation of the mean RDF values in the last 10 ns versus distance from COM of BCD is plotted in Figure 6. According to this figure, the maximum distribution of LVDP is observed at 0.57 nm from COM–BCD (blue curve). The distribution of water molecules around BCD in the absence (green graph) and presence (purple graph) of LVDP represents a significant amount of water in the hydrophobic cavity of BCD in the

absence of LVDP. However, most of these water molecules have been displaced by LVDP due to the insertion of LVDP into the hydrophobic cavity of BCD and the formation of the complex.

The comparison of green and purple diagrams in Figure 6 represents the increase of water distribution in the presence of LVDP in the cavity of BCD. This observation could be related to the amino group of LVDP that interacts with water molecules via hydrogen bonds. The  $R_s$  of BCD–LVDP can be estimated from the intersection point of blue and green diagrams.<sup>64</sup> The intersection point appears at 0.73 nm, which agrees with  $R_s'$  obtained value from the previous section. According to the water distribution diagram around BCD (green), the radius of the outer water layer ( $R_o$ ) is about 1.49 nm. The comparison of  $R_s$  and  $R_o$  values of BCD in the presence and absence of LVDP (Table 3) represents the compaction of BCD due to complexation with LVDP.

**Table 3.** Effective Radius of Gyration ( $R_s$ ) and Radius of Outer ( $R_o$ ) of BCD in the Absence and Presence of LVDP

radius (nm)	BCD–LVDP	free BCD
$R_s$	0.73	0.78 <sup>a</sup>
$R_o$	1.49	1.53 <sup>a</sup>

<sup>a</sup>These data have been taken from the literature.<sup>65</sup>

The Lenard-Jones interaction energy ( $E_{LJ}$ ) is also calculated during the MD simulation. The mean values of  $E_{LJ}$  in the last 10 ns of simulation are +1.6, –2.1, and –20.7 kcal/mol for LVDP–water, LVDP–LVDP, and BCD–LVDP, respectively. These results show that the formation of the BCD–LVDP complex is favorable from the viewpoint of  $E_{LJ}$ . Also, in other studies to investigate the ratio of BCD and LVDP for complexation, in the presence of a BCD and several LVDPs, the result shows an average ratio of 1:1.

Another critical analysis between LVDP and its environment is the hydrogen bond. By setting 0.35 nm and 10° for the cutoff radius and cutoff angle, respectively, the values of 3 and

7 are obtained for the average number of hydrogen bonds between LVDP–BCD and LVDP–water molecules, respectively. The two oxygens of the carboxylic groups and the oxygen of the phenolic group in LVDP, as hydrogen acceptors, and three OH groups of BCD, as hydrogen donors, formed these hydrogen bonds between LVDP and BCD. The locations of these hydrogen bonds are shown in Figure 7. Figure 8 shows

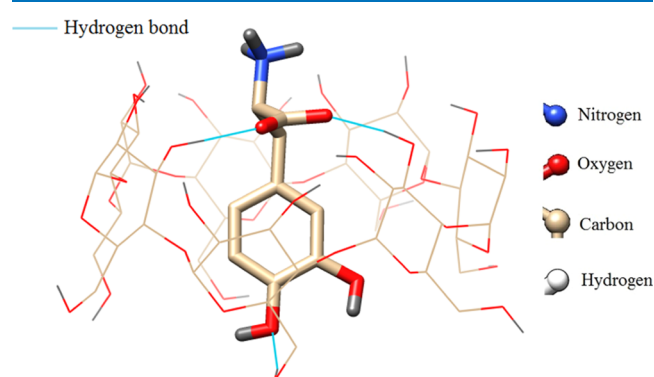


**Figure 7.** Scheme of the BCD–LVDP complex. The most probable hydrogen bonds between LVDP and BCD are dedicated by blue lines.

the RDF diagrams for  $-N-H\cdots O(\text{water})$ ,  $-\text{phenolic}-H\cdots O(\text{water})$ , and  $-\text{phenolic}-O\cdots H(\text{water})$  as the most probable hydrogen bonds between LVDP and water molecules. According to this figure, the relative contribution of these bonds to the total number of the hydrogen bonds is 3:3:1. The higher contribution of  $-N-H\cdots O(\text{water})$  and  $-\text{phenolic}-H\cdots O(\text{water})$  could be related to the positive charge of the amine group and higher availability of the  $-\text{phenolic}-H$  group.

As mentioned before, one of the most common analyses, conducted by umbrella sampling simulations, is the PMF extraction, which yields the  $\Delta G$  for the binding and unbinding processes. The optimized structure of the BCD–LVDP complex, from the previous stage by 100 ns MD production, was considered the starting point. LVDP is moved from its

equilibrium position in the  $Z$ -axis direction at a speed of 0.01 nm/ps during a 200 ps time evolution, and 400 frames were extracted. As the  $X$ - and  $Y$ -axis displacements do not significantly change the potential, the movement in these directions has not been considered. The distance between COM–LVDP and COM–BCD was measured for these 400 frames. Subsequently, the 38 frames were selected by a 0.05 nm changing distance for the umbrella sampling stage. Then, each frame was simulated using 1 ns in the  $NPT$  ensemble for equilibration and 10 ns in MD production. The calculated PME values using WHAM analysis are shown in Figure 9. The difference between the lowest and highest values of PME is about  $-3.67 \pm 0.05$  kcal/mol, which is a reasonable estimation for the BCD–LVDP binding energy obtained.<sup>44</sup>

In the last part of this work, we focus on the results of the QM/MM method for the geometrical structure, dynamics properties, IR spectra, and energy parameters of the LVDP–BCD complex. The time evolution of distance between COM of LVDP and BCD, as a structural parameter, was calculated by MD and QM/MM methods, and the results are shown in Figure 10. The average distances between the COM of LVDP and BCD in the last 20 ns of MD and the last 5 ns of QM/MM are about 0.12 and 0.09 nm, respectively. By considering the experimental value, 0.10 nm, obtained from the X-ray structure,<sup>19</sup> QM/MM leads to a more accurate result.

The time evolution of  $\theta$  and  $\varphi$  dihedral angles, as other structure properties, has been evaluated for 200 snapshots of the last 5 ns of QM/MM calculations, and the results are shown in Figure 11, representing the higher degree of freedom. In order to estimate the most probable range of  $\theta$  and  $\varphi$ , their normal distribution functions are evaluated and shown in Figure 12. The most probable value for  $\theta$  is observed at  $\pm 24^\circ$ , while that for  $\varphi$  is observed at  $28^\circ$ . The  $\theta$  value dispersion is much higher, representing its higher degree of freedom.

As mentioned before, the study and assay of spectroscopic spectra such as IR is one of the most compelling cases in computational studies and covers a wide range of studies. In this study, we intend to investigate the effects of the solvent

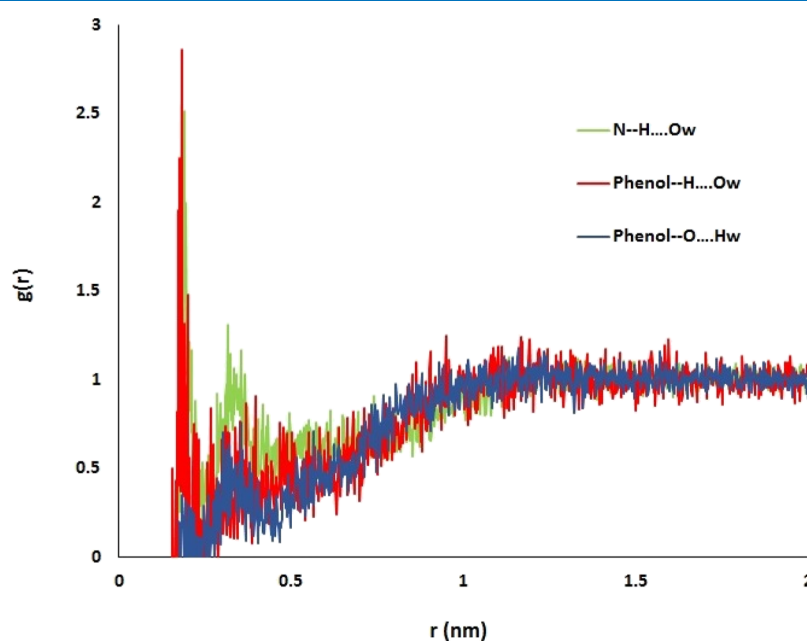


**Figure 8.** Normal RDF calculation for hydrogen bonds of LVDP with bulk water.

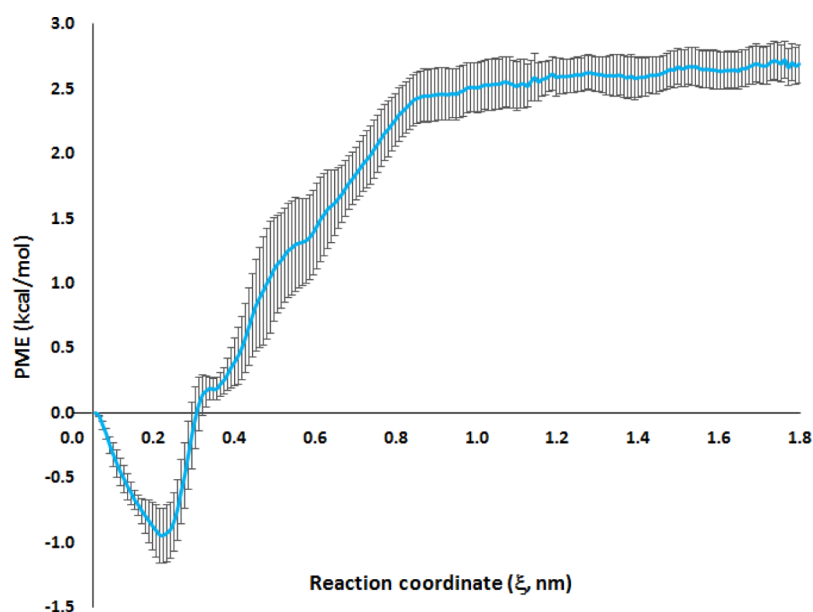


Figure 9. PMF diagram for the BCD–LVDP complex.

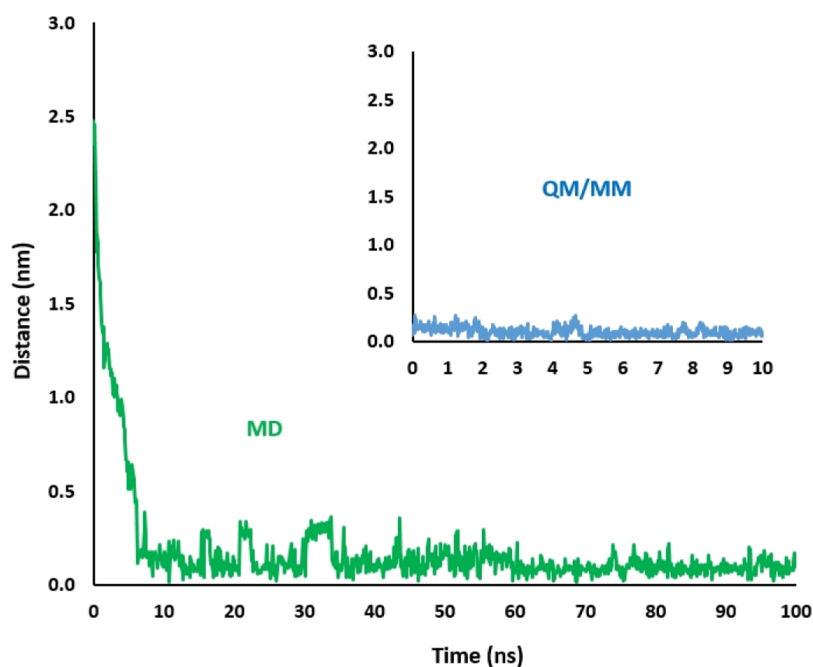


Figure 10. Time evolution of the distance for the 100 ns MD and 10 ns QM/MM (inner diagram) for the BCD–LVDP complex.

and mainly hydrogen bonding on LVDP in the presence of BCD. Figure 4 shows the characteristic peaks of the gas-phase LVDP in BCD, labeled with a to f, and for free LVDP in the aqueous phase, labeled with a' and d'. The IR spectrum of the LVDP–BCD complex has been calculated based on QM/MM, and the integrated nonscaled frequencies are shown in Table 4. The differences between the obtained values from the gas-phase calculations and QM/MM could be related to the solvation and hydrogen bonds. For instance, the estimated frequency of C=O bound in LVDP from QM/MM is  $1670\text{ cm}^{-1}$ , while the value in the gas phase is  $1846\text{ cm}^{-1}$ , which is due to the formation of a hydrogen bond with the water molecule and interactions with BCD (peak d). The difference between d ( $1670\text{ cm}^{-1}$ ) and d' ( $1658\text{ cm}^{-1}$ ) values represents the less hydration of C=O in the BCD cavity. We could

provide the same interpretation for the phenolic O–H group of LVDP from QM/MM ( $3552\text{ cm}^{-1}$ ) and gas-phase calculations ( $3801\text{ cm}^{-1}$ ). However, the relatively high difference between a ( $3552\text{ cm}^{-1}$ ) and a' ( $3795\text{ cm}^{-1}$ ) represents the weakness of the QM method in accounting for the solvation effect.

The estimation of the binding energy is the last part of this endeavor. There are two approaches for this purpose; in the first, the average energy of free BCD ( $\langle E_{\text{QM/MM}}^{\text{BCD}} \rangle$ ), LVDP ( $\langle E_{\text{QM/MM}}^{\text{levodopa}} \rangle$ ), and BCD–LVDP ( $\langle E_{\text{QM/MM}}^{\text{complex}} \rangle$ ) in the aqueous media is estimated using the QM/MM level, and the average binding energy is calculated according to the following equation:<sup>24</sup>

$$E_{\text{QM/MM}} = \langle E_{\text{QM/MM}}^{\text{complex}} \rangle - \langle E_{\text{QM/MM}}^{\text{BCD}} \rangle - \langle E_{\text{QM/MM}}^{\text{levodopa}} \rangle \quad (2)$$

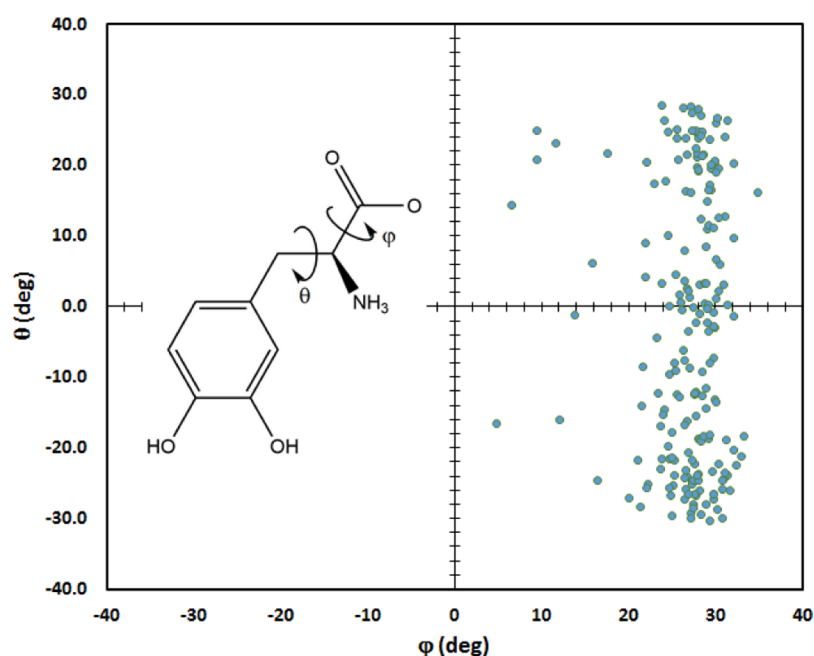


**Figure 11.** Time evolution of  $\theta$  and  $\phi$  dihedral angles (dynamics) for the last 5 ns of the QM/MM method. We have not shown the whole data (5000 points) and just selected 200 for the presentation.

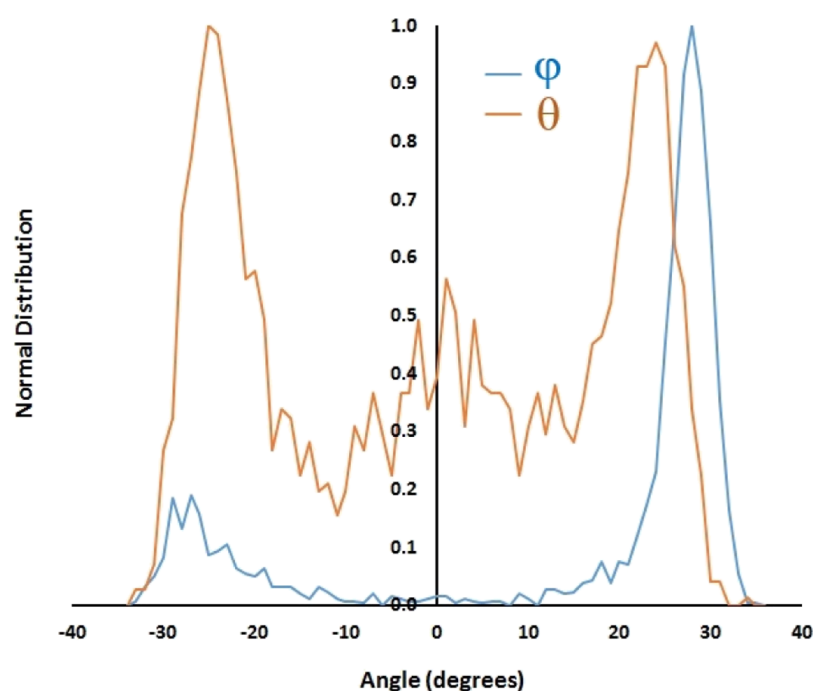


**Figure 12.** Normal distribution of  $\theta$  and  $\phi$  dihedral angles for the last 5 ns of the QM/MM method. The whole data (5000 points) have been used for production of this diagram.

The average energy for each component has been calculated over 200 structures (200 snapshots) extracted from the last 5 ns of QM/MM simulation in an explicit water solvent. The estimated average energy values for LVDP, BCD, and BCD-LVDP are  $-2704.4 \pm 0.8$ ,  $-14631.3 \pm 0.7$ , and  $-17339.4 \pm 0.7$  kcal/mol, respectively. By considering these quantities and using eq 2, the value of  $-3.75 \pm 0.01$  kcal/mol is obtained. As explained in the section on Computational Methods, the main shortcoming of this method is ignoring entropy contribution.

In the second approach, the binding energy has been estimated using the QM/MM/PBSA method, where the

entropy contribution is brought up. The estimated binding energy from this approach is  $-4.14$  kcal/mol. According to eq 1, the estimated values of the energy components from the QM/MM/PBSA method are listed in Table 5.

A comparison among the estimated binding energy values obtained from the considered methods and their deviation from the experimental value is provided in Table 6. According to the results, the following order is extracted for the accuracy of the methods:

$Q_{M, \text{Gas phase}} < Q_{M, \text{Implicit water}} < \text{SMD} \approx \approx Q_{M/MM} \ll Q_{M/MM/PBSA}$ . While the highest accuracy refers to QM/MM/

**Table 4.** Comparison of the Calculated Absorption Frequencies in the IR Spectrum of BCD–LVDP and LVDP in the Aqueous Phase by QM and QM/MM Methods

peak	bond	groups	LVDP (aqueous) QM freq. <sup>a</sup>	BCD–LVDP QM freq. <sup>a</sup>	BCD–LVDP QM/MM freq. <sup>a</sup>
a, a'	O–H stretching	phenol	3795	3801	3552
b	O–H stretching	carboxylic		3722	
c	C–H stretching	aromatic	3160	3129	3061
d, d'	C=O stretching	carboxylic	1658	1846	1670
e	N–H bending	amide	1605	1733	1628
f	C=C stretching	aromatic	1551	1600	1525

<sup>a</sup>All frequencies are in cm<sup>-1</sup> units.

**Table 5.** Values of Energy Contribution (kcal/mol) for the Formation of the BCD–LVDP Complex Obtained from the QM/MM/PBSA Method

$\Delta E_{\text{complex, vdw}}$	$\Delta E_{\text{complex, ele}}$	$\Delta E_{\text{sol, polar}}$	$\Delta E_{\text{sol, nonpolar}}$	$-T\Delta S$	$\Delta G_{\text{binding}}$
-14.54(±0.04)	-10.36(±0.25)	+21.86(±0.32)	-1.78(±0.03)	+0.68(±0.01)	-4.14(±0.41)

**Table 6.** Values of Binding Free Energy for the Formation of the BCD–LVDP Complex, Obtained from Various Computational Methods Such as QM, SMD, QM/MM, and QM/MM/PBSA, and Their Percent of Deviation (Dev. %) from the Experimental Value

method	QM gas phase	QM implicit water	SMD	QM/MM	QM/MM/PBSA	experimental
$\Delta G_{\text{binding}}$ (kcal/mol)	+0.03	-1.57	-3.67	-3.75	-4.14	-4.25 <sup>a</sup>
Dev. %	100.7%	63%	14%	12%	2.6%	

<sup>a</sup>These data have been taken from ref 16.

PBSA, it has the highest computational cost. The more accuracy of QM/MM/PBSA concerning QM/MM represents that the addition of PBSA analysis leads to more realistic results that could be due to the importance of solvation. Interestingly, the difference between SMD and QM/MM results is not significant, while the computational cost of QM/MM is much higher.

Different computational methods can complement each other well. In other words, each of these methods can be useful in such a way. For example, in this study, a quantum method was performed to extract drug and carrier parameters (such as length, angle, and partial charge) and the initial guess of the interaction orientation using an MEP. According to Figure S1a, it can be predicted that the inner surface of BCD has hydrophobic properties, and the phenolic group of LVDP shows hydrophobicity. Therefore, it is more probable that the drug molecule will approach the inner surface of BCD from the phenolic group, which is consistent with the results obtained from the MD simulation. The NBO analysis shows three significant charge transfers between BCD and LVDP, representing the minor role of hydrogen bonds and the predominant role of electrostatic interactions in the binding energy. At the same time, the MD calculations lead to the result of more contribution of hydrogen bonds. The obtained structural properties (the distance between COM and dihedral angles) from MD and the hybrid method are very close to the experimental values, representing the close accuracy of these methods for estimating the structural parameters. However, the QM method does not provide a reasonable estimate. While SMD does not provide the MD features, it is considered a complementary method (MD/SMD) in calculating the binding energy.

#### 4. CONCLUSIONS

This work focuses on the molecular aspects of BCD–LVDP interactions using various computational techniques with

different advantages and disadvantages. This strategy provided a comprehensive perspective of this system. The comparison of properties such as chemical potential, energy gap, and binding energy in the QM method for both gas and aqueous phases represents the higher stability of LVDP in the aqueous phase due to electrostatic interactions. The QM method also predicts the presence of only two weak hydrogen bonds between LVDP and BCD in the aqueous phase, which belong to the LVDP phenolic groups, and does not provide any information about the other possible hydrogen bonds that may be formed by amine and carboxylic groups. Moreover, this method does not assign the apparent arrangement of the amino and carboxylic groups of LVDP in the BCD cavity, could not estimate the accurate IR frequency bands, and could not provide a realistic picture of the solvent effects and hydrogen bonds. The MD calculations with the explicit water model ran in the next part of this endeavor to overcome these deficiencies. The results of MD calculations indicate the formation of a 1:1 complex with a suitable internal and external radius that certifies the ability of the complex to cross the blood–brain barrier. The location of LVDP at the center of BCD, the significant role of hydrogen bonds in the complex formation, the highest distribution of water molecules around the amino and phenolic groups of LVDP, and the enhancement of water solubility of LVDP in the presence of the BCD are the other results of the MD calculations.

The RDF analysis represents the water molecule's removal from the cavity and the redistribution around BCD due to the insertion of LVDO. This observation led us to account for the effects of hydrophilicity and hydrophobicity on the binding energy using QM/MM/PBSA as a more precise and accurate method. The value of -4.14 kcal/mol is estimated for the binding energy from QM/MM/PBSA calculations. Moreover, the results represent the higher contribution of the hydrophobic effect concerning the hydrophilic effect in the binding energy.

As the QM/MM method reasonably considers the dipolar effects of water and hydrogen bonding, a more accurate IR spectrum of the complex is estimated from QM/MM calculations. Moreover, by considering the precise arrangement of carboxylic and amine functional groups, QM/MM assigns a higher number of strong hydrogen bonds between LVDP and BCD. However, the MD method's estimated values are not reliable due to the high fluctuations.

## ■ ASSOCIATED CONTENT

### Supporting Information

The Supporting Information is available free of charge at <https://pubs.acs.org/doi/10.1021/acsomega.1c02637>.

Molecular electrostatic potential map of BCD and LVDP, visualization of BCD–LVDP, and some major charge transfers in BCD–LVDP (PDF)

## ■ AUTHOR INFORMATION

### Corresponding Author

Abdol-Khalegh Bordbar – Department of Chemistry, University of Isfahan, Isfahan 8174673441, Iran; Present Address: California Institute for Quantitative Biosciences (QB3), University of California, Berkeley, USA; [orcid.org/0000-0002-0492-8979](https://orcid.org/0000-0002-0492-8979); Phone: +1(408) 594 6952; Email: [akbordbar@berkeley.edu](mailto:akbordbar@berkeley.edu), [akbordbar@gmail.com](mailto:akbordbar@gmail.com)

### Authors

Morteza Rezaeisadat – Department of Chemistry, University of Isfahan, Isfahan 8174673441, Iran  
Nafiseh Salehi – Department of Chemistry, University of Isfahan, Isfahan 8174673441, Iran

Complete contact information is available at: <https://pubs.acs.org/doi/10.1021/acsomega.1c02637>

### Notes

The authors declare no competing financial interest.

## ■ ACKNOWLEDGMENTS

The financial support of the Research Council of Isfahan University is kindly acknowledged.

## ■ REFERENCES

- (1) Sadek, R. M.; Mohammed, S. A.; Abunbehan, A. R. K.; Ghattas, A. K. H. A.; Badawi, M. R.; Mortaja, M. N.; Abu-Nasser, B. S.; Abu-Naser, S. S. Parkinson's Disease Prediction Using Artificial Neural Network. *Int. J. Acad. Health Med. Res.* **2019**, *3*, 1.
- (2) Tysnes, O.-B.; Storstein, A. Epidemiology of Parkinson's Disease. *J. Neural Transm.* **2017**, *124*, 901–905.
- (3) Freitas, M. E.; Ruiz-Lopez, M.; Fox, S. H. Novel Levodopa Formulations for Parkinson's Disease. *CNS Drugs* **2016**, *30*, 1079–1095.
- (4) Carlsson, A. Treatment of Parkinson's with L-DOPA. The Early Discovery Phase, and a Comment on Current Problems. *J. Neural Transm.* **2002**, *109*, 777–787.
- (5) Fahn, S. Levodopa in the Treatment of Parkinson's Disease. In *Oxidative Stress and Neuroprotection*; Springer, 2006; pp 1–15.
- (6) Tarakad, A.; Jankovic, J. Diagnosis and Management of Parkinson's Disease. *Seminars in neurology*; Thieme Medical Publishers, 2017; Vol. 37, pp 118–126.
- (7) Mizuno, Y.; Shimoda, S.; Origasa, H. Long-Term Treatment of Parkinson's Disease with Levodopa and Other Adjunctive Drugs. *J. Neural Transm.* **2018**, *125*, 35–43.

- (8) Schapira, A. H. V.; Fox, S. H.; Hauser, R. A.; Jankovic, J.; Jost, W. H.; Kenney, C.; Kulisevsky, J.; Pahwa, R.; Poewe, W.; Anand, R. Assessment of Safety and Efficacy of Safinamide as a Levodopa Adjunct in Patients with Parkinson Disease and Motor Fluctuations: A Randomized Clinical Trial. *JAMA Neurol.* **2017**, *74*, 216–224.
- (9) Jain, K. K. Drug Delivery Systems - An Overview. *Drug Delivery Systems*; Springer, 2008; pp 1–50.
- (10) Shahwal, V. K.; Upadhyay, A. Gastro-Retentive Floating Drug Delivery Systems. *Int. J. Biomed. Res.* **2011**, *2*, 381.
- (11) Deb, P. K.; Kokaz, S. F.; Abed, S. N.; Paradkar, A.; Tekade, R. K. Pharmaceutical and Biomedical Applications of Polymers. *Basic Fundam. Drug Delivery* **2019**, 203–267.
- (12) Reddy, M. N.; Rehana, T.; Ramakrishna, S.; Chowdary, K. P. R.; Diwan, P. V.  $\beta$ -Cyclodextrin Complexes of Celecoxib: Molecular-Modeling, Characterization, and Dissolution Studies. *AAPS PharmSci* **2004**, *6*, 68–76.
- (13) Vyas, A.; Saraf, S.; Saraf, S. Cyclodextrin Based Novel Drug Delivery Systems. *J. Inclusion Phenom. Macrocyclic Chem.* **2008**, *62*, 23–42.
- (14) Karande, P.; Mitragotri, S. Enhancement of Transdermal Drug Delivery via Synergistic Action of Chemicals. *Biochim. Biophys. Acta, Biomembr.* **2009**, *1788*, 2362–2373.
- (15) Kiss, T.; Alapi, T.; Varga, G.; Bartos, C.; Ambrus, R.; Szabó-Révész, P.; Katona, G. Interaction Studies between Levodopa and Different Excipients to Develop Coground Binary Mixtures for Intranasal Application. *J. Pharm. Sci.* **2019**, *108*, 2552–2560.
- (16) Barros, M. C. F.; Ribeiro, A. C. F.; Estes, M. A. Cyclodextrins in Parkinson's Disease. *Biomolecules* **2019**, *9*, 3–18.
- (17) Cui, Q. Perspective: Quantum Mechanical Methods in Biochemistry and Biophysics. *J. Chem. Phys.* **2016**, *145*, 140901.
- (18) Jensen, F. *Introduction to Computational Chemistry*; John Wiley & Sons, 2017.
- (19) Obaidat, R.; Al-Shar'i, N.; Tashtoush, B.; Athamneh, T. Enhancement of Levodopa Stability When Complexed with  $\beta$ -Cyclodextrin in Transdermal Patches. *Pharm. Dev. Technol.* **2018**, *23*, 986–997.
- (20) Al-Shar'i, N. A.; Obaidat, R. M. Experimental and Computational Comparative Study of the Supercritical Fluid Technology (SFT) and Kneading Method in Preparing  $\beta$ -Cyclodextrin Complexes with Two Essential Oils (Linalool and Carvacrol). *AAPS PharmSci-Tech* **2018**, *19*, 1037–1047.
- (21) Fateminasab, F.; Bordbar, A. K.; Shityakov, S.; Saboury, A. A. Molecular Insights into Inclusion Complex Formation between  $\beta$ - and  $\gamma$ -Cyclodextrins and Rosmarinic Acid. *J. Mol. Liq.* **2020**, *314*, 113802.
- (22) Shityakov, S.; Salmas, R. E.; Durdagi, S.; Roewer, N.; Förster, C.; Broscheit, J. Solubility Profiles, Hydration and Desolvation of Curcumin Complexed with  $\gamma$ -Cyclodextrin and Hydroxypropyl- $\gamma$ -Cyclodextrin. *J. Mol. Struct.* **2017**, *1134*, 91–98.
- (23) Shityakov, S.; Broscheit, J.; Förster, C.  $\alpha$ -Cyclodextrin Dimer Complexes of Dopamine and Levodopa Derivatives to Assess Drug Delivery to the Central Nervous System: ADME and Molecular Docking Studies. *Int. J. Nanomed.* **2012**, *7*, 3211.
- (24) Khandelwal, A.; Lukacova, V.; Comez, D.; Kroll, D. M.; Raha, S.; Balaz, S. A Combination of Docking, QM/MM Methods, and MD Simulation for Binding Affinity Estimation of Metalloprotein Ligands. *J. Med. Chem.* **2005**, *48*, 5437–5447.
- (25) Karaman, R.; Fattash, B.; Qtaib, A. The Future of Prodrugs—Design by Quantum Mechanics Methods. *Expert Opin. Drug Delivery* **2013**, *10*, 713–729.
- (26) David, C. Y. *Computational Chemistry*; John Wiley & Sons, 2001.
- (27) Kim, S.; Chen, J.; Cheng, T.; Gindulyte, A.; He, J.; He, S.; Li, Q.; Shoemaker, B. A.; Thiessen, P. A.; Yu, B.; Zaslavsky, L.; Zhang, J.; Bolton, E. E. PubChem 2019 Update: Improved Access to Chemical Data. *Nucleic Acids Res.* **2019**, *47*, D1102–D1109.
- (28) Yanai, T.; Tew, D. P.; Handy, N. C. A New Hybrid Exchange–Correlation Functional Using the Coulomb-Attenuating Method (CAM-B3LYP). *Chem. Phys. Lett.* **2004**, *393*, 51–57.

- (29) Vydrov, O. A.; Heyd, J.; Krukau, A. V.; Scuseria, G. E. Importance of Short-Range versus Long-Range Hartree-Fock Exchange for the Performance of Hybrid Density Functionals. *J. Chem. Phys.* **2006**, *125*, 074106.
- (30) Dunning, T. H., Jr. Gaussian Basis Sets for Use in Correlated Molecular Calculations. I. The Atoms Boron through Neon and Hydrogen. *J. Chem. Phys.* **1989**, *90*, 1007–1023.
- (31) Barone, V.; Cossi, M.; Tomasi, J. Geometry Optimization of Molecular Structures in Solution by the Polarizable Continuum Model. *J. Comput. Chem.* **1998**, *19*, 404–417.
- (32) Frisch, M.; Trucks, G. W.; Schlegel, H. B.; Scuseria, G. E.; Robb, M. A.; Cheeseman, J. R.; Scalmani, G.; Barone, V.; Mennucci, B.; Petersson, G. *Gaussian 09*, Revision d. 01; Gaussian Inc.: Wallingford CT, 2009, 201.
- (33) Hanwell, M. D.; Curtis, D. E.; Lonie, D. C.; Vandermeersch, T.; Zurek, E.; Hutchison, G. R. Avogadro: An Advanced Semantic Chemical Editor, Visualization, and Analysis Platform. *J. Cheminf.* **2012**, *4*, 17.
- (34) Dennington, R.; Keith, T. A.; Millam, J. M. *GaussView*, version 6; Semichem Inc, 2016.
- (35) Pettersen, E. F.; Goddard, T. D.; Huang, C. C.; Couch, G. S.; Greenblatt, D. M.; Meng, E. C.; Ferrin, T. E. UCSF Chimera—a Visualization System for Exploratory Research and Analysis. *J. Comput. Chem.* **2004**, *25*, 1605–1612.
- (36) Pronk, S.; Páll, S.; Schulz, R.; Larsson, P.; Bjelkmar, P.; Apostolov, R.; Shirts, M. R.; Smith, J. C.; Kasson, P. M.; van der Spoel, D.; Hess, B.; Lindahl, E. GROMACS 4.5: a high-throughput and highly parallel open source molecular simulation toolkit. *Bioinformatics* **2013**, *29*, 845–854.
- (37) Hornak, V.; Abel, R.; Okur, A.; Strockbine, B.; Roitberg, A.; Simmerling, C. Comparison of Multiple Amber Force Fields and Development of Improved Protein Backbone Parameters. *Proteins: Struct., Funct., Bioinf.* **2006**, *65*, 712–725.
- (38) Hoover, W. G. Canonical dynamics: Equilibrium phase-space distributions. *Phys. Rev. A: At., Mol., Opt. Phys.* **1985**, *31*, 1695–1697.
- (39) Humphrey, W.; Dalke, A.; Schulten, K. VMD: Visual Molecular Dynamics. *J. Mol. Graphics* **1996**, *14*, 33–38.
- (40) Case, D. A.; Ben-Shalom, I. Y.; Brozell, S. R.; Cerutti, D. S.; Cheatham, T. E., III; Cruzeiro, V. W. D.; Darden, T. A.; Duke, R. E.; Ghoreishi, D.; Gilson, M. K.; Gohlke, H.; Goetz, A. W.; Greene, D.; Harris, R.; Homeyer, N.; Izadi, S.; Kovalenko, A.; Kurtzman, T.; Lee, T. S.; LeGra, S. *AmberTools18*; University of California: San Francisco, 2018.
- (41) Bussi, G.; Donadio, D.; Parrinello, M. Canonical Sampling through Velocity Rescaling. *J. Chem. Phys.* **2007**, *126*, 014101.
- (42) Berendsen, H. J. C.; Postma, J. P. M.; van Gunsteren, W. F.; DiNola, A.; Haak, J. R. Molecular Dynamics with Coupling to an External Bath. *J. Chem. Phys.* **1984**, *81*, 3684–3690.
- (43) Essmann, U.; Perera, L.; Berkowitz, M. L.; Darden, T.; Lee, H.; Pedersen, L. G. A Smooth Particle Mesh Ewald Potential. *J. Chem. Phys.* **1995**, *103*, 8577–8593.
- (44) Hess, B.; Bekker, H.; Berendsen, H. J. C.; Fraaije, J. G. E. M. LINCS: A Linear Constraint Solver for Molecular Simulations. *J. Comput. Chem.* **1997**, *18*, 1463–1472.
- (45) Kästner, J. Umbrella Sampling. *Wiley Interdiscip. Rev.: Comput. Mol. Sci.* **2011**, *1*, 932–942.
- (46) Virnau, P.; Müller, M. Calculation of Free Energy through Successive Umbrella Sampling. *J. Chem. Phys.* **2004**, *120*, 10925–10930.
- (47) Chodera, J. D.; Swope, W. C.; Pitera, J. W.; Seok, C.; Dill, K. A. Use of the Weighted Histogram Analysis Method for the Analysis of Simulated and Parallel Tempering Simulations. *J. Chem. Theory Comput.* **2007**, *3*, 26–41.
- (48) Neese, F. Software Update: The ORCA Program System, Version 4.0. *Wiley Interdiscip. Rev.: Comput. Mol. Sci.* **2018**, *8*, No. e1327.
- (49) Senn, H. M.; Thiel, W. QM/MM Methods for Biomolecular Systems. *Angew. Chem., Int. Ed.* **2009**, *48*, 1198–1229.
- (50) Ahmadi, S.; Barrios Herrera, L.; Chehelamirani, M.; Hostaš, J.; Jalife, S.; Salahub, D. R. Multiscale Modeling of Enzymes: QM-cluster, QM/MM, and QM/MM/MD: A Tutorial Review. *Int. J. Quantum Chem.* **2018**, *118*, No. e25558.
- (51) Murphy, R. B.; Philipp, D. M.; Friesner, R. A. A Mixed Quantum Mechanics/Molecular Mechanics (QM/MM) Method for Large-scale Modeling of Chemistry in Protein Environments. *J. Comput. Chem.* **2000**, *21*, 1442–1457.
- (52) Kollman, P. A.; Massova, I.; Reyes, C.; Kuhn, B.; Huo, S.; Chong, L.; Lee, M.; Lee, T.; Duan, Y.; Wang, W.; Donini, O.; Cieplak, P.; Srinivasan, J.; Case, D. A.; Cheatham, T. E. Calculating Structures and Free Energies of Complex Molecules: Combining Molecular Mechanics and Continuum Models. *Acc. Chem. Res.* **2000**, *33*, 889–897.
- (53) Barone, V.; Cossi, M.; Tomasi, J. A New Definition of Cavities for the Computation of Solvation Free Energies by the Polarizable Continuum Model. *J. Chem. Phys.* **1997**, *107*, 3210–3221.
- (54) Chidangil, S.; Shukla, M. K.; Mishra, P. C. A Molecular Electrostatic Potential Mapping Study of Some Fluoroquinolone Anti-Bacterial Agents. *Mol. Model. Annual* **1998**, *4*, 250–258.
- (55) dos Santos, M. A. B.; de Oliveira, L. F. S.; de Figueiredo, A. F.; dos Santos Gil, F.; de Souza Farias, M.; Bitencourt, H. R.; Lobato, J. R. B.; Ferreira, R. D. de P.; Alvesda, S. S. S.; de Aquino, E. L. C. Molecular Electrostatic Potential and Chemometric Techniques as Tools to Design Bioactive Compounds. *Cheminformatics and Its Applications*; IntechOpen, 2019.
- (56) Pavia, D. L.; Lampman, G. M.; Kriz, G. S.; Vyvyan, J. A. *Introduction to Spectroscopy*; Cengage Learning, 2008.
- (57) Edwin, B.; Hubert Joe, I. Vibrational Spectral Analysis of Anti-Neurodegenerative Drug Levodopa: A DFT Study. *J. Mol. Struct.* **2013**, *1034*, 119–127.
- (58) Dixit, S. B.; Ponomarev, S. Y.; Beveridge, D. L. Root Mean Square Deviation Probability Analysis of Molecular Dynamics Trajectories on DNA. *J. Chem. Inf. Model.* **2006**, *46*, 1084–1093.
- (59) Lobanov, M. I.; Bogatyreva, N. S.; Galzitskaia, O. V. Radius of Gyration Is Indicator of Compactness of Protein Structure. *Mol. Biol.* **2008**, *42*, 701–706.
- (60) Chen, S. H. Small Angle Neutron Scattering Studies of the Structure and Interaction in Micellar and Microemulsion Systems. *Annu. Rev. Phys. Chem.* **1986**, *37*, 351–399.
- (61) Rezaeisadat, M.; Bordbar, A.-K.; Omidyan, R. Molecular Dynamics Simulation Study of Curcumin Interaction with Nano-Micelle of PNIPAAm-b-PEG Co-Polymer as a Smart Efficient Drug Delivery System. *J. Mol. Liq.* **2021**, *332*, 115862.
- (62) Lee, B.; Richards, F. M. The Interpretation of Protein Structures: Estimation of Static Accessibility. *J. Mol. Biol.* **1971**, *55*, 379.
- (63) Durham, E.; Dorr, B.; Woetzel, N.; Staritzbichler, R.; Meiler, J. Solvent Accessible Surface Area Approximations for Rapid and Accurate Protein Structure Prediction. *J. Mol. Model.* **2009**, *15*, 1093–1108.
- (64) Mobasheri, M.; Attar, H.; Rezayat Sorkhabadi, S.; Khamesipour, A.; Jaafari, M. Solubilization Behavior of Polyene Antibiotics in Nanomicellar System: Insights from Molecular Dynamics Simulation of the Amphotericin B and Nystatin Interactions with Polysorbate 80. *Molecules* **2016**, *21*, 6.
- (65) Gidwani, B.; Vyas, A. A Comprehensive Review on Cyclodextrin-Based Carriers for Delivery of Chemotherapeutic Cytotoxic Anticancer Drugs. *BioMed Res. Int.* **2015**, *2015*, 198268.